The influence of defect structure changes at phase transition on electrical properties in the $Bi_{0.75}Pr_{0.25}O_{1.5}$ oxide ion conductor

J. Jamroz,[1] M. Malys,[1] F. Krok,[1] J. Maier,[2] A. Kyriacou,[3] S. J. Ahmed,[3] I. Abrahams,[3*] W. Wrobel[1*]

[1]Faculty of Physics, Warsaw University of Technology, Koszykowa75, 00-662 Warszawa, Poland.

[2]Max Planck Institute for Solid State Research, 70569 Stuttgart, Germany

[3]Materials Research Institute, School of Biological and Chemical Sciences, Queen Mary University of London, Mile End Road, London E1 4NS, U.K.

Corresponding authors:

i.abrahams@qmul.ac.uk

wojciech.wrobel@pw.edu.pl

Abstract

The structural properties of $Bi_{0.75}Pr_{0.25}O_{1.5}$ have been investigated by powder X-ray and neutron diffraction as a function of temperature up to around 800 °C. A layered rhombohedral structure is confirmed throughout the temperature range studied, with an order-disorder type phase transition ($\beta_2 \leftrightarrow \beta_1$) at *ca.* 730 °C. This transition is accompanied by partial migration of the oxide ions from the fluorite-like blocks of the layered structure to interstitial sites in the van der Waals gap between blocks. A reversible step change in total conductivity, associated with the phase transition, is preceded by non-linear behaviour observed in the Arrhenius plot of total conductivity at lower temperatures. A theoretical model based on a modification of the "cube-root" model successfully describes the conductivity data through the phase transition, showing the transition to involve a jump in inter-planar conductivity correlated with the appearance of interstitial oxide ions in the van der Waals gap. While the "cube root" model has been successfully used to explain phase transitions in classic 3-dimensional ionic conductors, the present study represents the first example of application of this model to a lower dimensional system.

Keywords:

Bismuth oxide, bismuth praseodymium oxide, rhombohedral structure, neutron diffraction, X-ray diffraction, a.c. impedance spectroscopy, transference numbers, cube-root model

1. Introduction

Solid oxides, with high values of oxide-ion conductivity at intermediate temperatures are being sought for new generations of solid oxide fuel cells, gas sensors and gas separation membranes. The high temperature δ-phase of Bi_2O_3 shows oxide-ion conductivity values in the order of 1 S cm^{-1} [1], the highest known oxide-ion conductivity of any solid. However, δ-Bi_2O_3 is only stable above around 730 °C, driving much research into stabilising this phase to lower temperatures through solid solution formation, typically with rare earth oxides [2–6].

These solid solutions often show either fully disordered defect fluorite structures, as in δ-Bi_2O_3, or ordered fluorite type phases. There has been much discussion in the literature on the stability of the substituted δ-Bi_2O_3 type phases [7]. Indeed, annealing of these phases at intermediate temperatures (around 600 °C) often leads to the formation of a stable rhombohedral phase. The rhombohedral phase can be formed directly when the substituting cation is large (e.g. Sr^{2+}, La^{3+}, Pr^{3+}, Nd^{3+} etc.) and usually shows appreciably high conductivity [8–10]. While cubic δ-type phases show 3-dimensional conduction pathways, the rhombohedral phase exhibits a layered structure, in which the conduction pathway is thought to be 2-dimensional. Indeed, significant disorder was noted on the anion sublattice of rhombohedral $Bi_{0.775}La_{0.225}O_{1.5}$ in a recent study by Ahi *et al*. [11]. These authors proposed that the main anionic conduction pathway was within the fluorite layers rather than between the layers.

The group of Drache have extensively studied the rhombohedral phases in Bi_2O_3-Ln_2O_3 systems [12–14]. The room temperature rhombohedral phase, denoted β_2, exhibits an incommensurate superlattice, the modulation vector of which differs in the La substituted system from most of the rare-earth substituted systems [15]. A phase transition from the low-temperature β_2 phase to a highly conducting disordered phase, β_1, is observed at around 700 °C [16]. For large lanthanides (e.g. La, Pr, Nd), a monoclinic distortion of the β_2 phase, termed ε, is obtained on annealing at around 300 °C [17]. Although this phase is closely related to the β_2 phase, the change in conductivity at the $\varepsilon \leftrightarrow \beta_2$ phase transition is more significant than at the $\beta_2 \leftrightarrow \beta_1$ transition, which is attributed to the relative activities of the Bi $6s^2$ lone pairs in these structures [18]. Conductivity measurements on single crystals of β_2-$Bi_{0.851}Sr_{0.149}O_{1.425}$ have confirmed that the conductivity in this system is essentially two-dimensional in nature [19].

Phase transitions, observed in various classic ionic conductors such as AgI, AgCl, AgBr and PbF_2, attract the interest of many research groups and both experimental and

theoretical works have been conducted to understand the relationship between changes in ionic conductivity and in defect distribution and / or concentration, in the vicinity of the phase transition. Several models utilize an excess chemical potential term, μ_{int}, associated with attractive defect interactions, to explain the anomalous increase of equilibrium defect concentration, *c*, at temperatures below the phase transition (most commonly $\mu_{\mathrm{int}} \sim c$ and/or $\mu_{\mathrm{int}} \sim c^{1/2}$) [20–22]. Although, these models appear to be helpful in the qualitative understanding of defect behavior in the pre-phase transition region, a quantitative description has been achieved only in the so called "cube-root" model [23], where the defect interaction term is modelled by the cube-root term ($\mu_{\mathrm{int}} \sim c^{1/3}$) related to the mean defect-defect distance in the defect containing sublattice. The cube-root model has been successfully applied to various classic 3-dimensional ionic conductors such as AgI, AgCl, AgBr and PbF_2 showing first or higher order phase transitions [24,25].

In this work we examine details of the $\beta_2 \leftrightarrow \beta_1$ transition in rhombohedral $Bi_{0.75}Pr_{0.25}O_{1.5}$, using a combination of X-ray and neutron diffraction and a.c. impedance spectroscopy. This compound shows excellent stability and relatively high oxide-ion conductivity in the order of 5×10^{-1} S cm^{-1} at 800 °C. A modification of the "cube-root" model is used here to link subtle changes in the defect structure to conductivity behaviour at the phase transition in order to provide a clearer picture of the mechanism at work during the phase transition. The present study represents the first example of application of this model to a lower dimensional system.

2. Experimental

2.1 Sample preparation

Samples of composition $Bi_{0.75}Pr_{0.25}O_{1.5}$ were prepared using stoichiometric amounts of Bi_2O_3 (Sigma Aldrich, 99.9%) and Pr_6O_{11} (Sigma Aldrich, 99.9%). The starting mixture was ground in ethanol using a planetary ball mill for 24 h. After drying, the green mixture was transferred to a platinum crucible and heated at 780 °C, then cooled and reground. The powder was then reheated to 850 °C for 24 h, before slow cooling to room temperature at a cooling rate of 2 °C min^{-1}. The resulting powder was yellow in colour.

For electrical measurements, the powder was subsequently reground and pelletised. Pellets were pressed isostatically at a pressure of 400 MPa, sintered at 850 °C for 10 h and then slow cooled in air to room temperature, at a cooling rate of 2 °C min^{-1}.

For neutron diffraction studies, samples were prepared using stoichiometric amounts of the starting materials which were ground in an agate mortar using methylated spirits as a dispersant. In each case the dried mixture was transferred to a platinum crucible and heated at 750 °C in a tube furnace for 24 h, then cooled and reground. The powder was then reheated at 800 °C for a further 24 h and then slow cooled in air.

2.2 Diffraction

X-ray powder diffraction data were collected on a Philips X'Pert Pro diffractometer, fitted with an X'Celerator detector, using Ni filtered Cu-Kα radiation (λ_1 = 1.54056 Å and λ_2 = 1.54439 Å). Room temperature data suitable for detailed Rietveld refinement were collected in the 2θ range 5-105°, in steps of 0.0167°, with an effective scan time of 250 s per step. Elevated temperature measurements were performed using an Anton-Paar HTK 1200 high temperature camera. Data were collected in flat plate θ/θ geometry on a Pt coated sample holder. Calibration was carried out with an external LaB_6 standard. Diffraction patterns were acquired at room temperature and at 50 °C intervals from 100 °C to 800 °C, over the range 5-105° 2θ, in steps of 0.033°, with an effective scan time of 50 s per step.

Neutron powder diffraction data were collected on the Polaris diffractometer at the ISIS Facility, Rutherford Appleton Laboratory. Data from back-scattering (130-160°) and low-angle (28-42°) detector banks were used in subsequent analysis. Room temperature data were collected on a sample contained in a cylindrical 7 mm diameter thin walled vanadium can, located in front of the back-scattering detectors. For elevated temperature measurements, the sample was sealed in a silica tube and placed inside a thin walled vanadium can. Data were collected at 50 °C intervals from 100 °C to 750 °C. Long data collections corresponding to proton beam currents of 1000 μA h and 200 μA h were made at room temperature and at 800 °C, respectively, with short data collections of 30 μA h carried out at all other temperatures. Structure refinement was performed with the GSAS suite of programmes [26], using a combined X-ray and neutron approach. The initial model was based on that of Drache *et al*. [10] in space group *R*-3*m*. Crystal and refinement parameters for $Bi_{0.75}Pr_{0.25}O_{1.5}$ at room temperature and 800 °C are given in the supporting information as Table S1. Structural graphics were prepared using VESTA [27].

2.3 Electrical measurements

Samples for impedance measurements were prepared as rectangular block (*ca.* $5 \times 3 \times 2$ mm^3) cut from slow cooled sintered pellets using a diamond saw. Platinum electrodes were sputtered by cathodic discharge. Electrical characterisation was carried out by a.c. impedance spectroscopy using a fully automated system based on a Solartron 1255 frequency response analyser in conjunction with a bespoke automatic current/voltage converter. Impedance data were collected over the frequency range 1 Hz to 1×10^6 Hz, in the approximate temperature range 200 to 800 °C. Impedance spectra were collected over cycles of heating and cooling at stabilised temperatures. Impedance at each frequency was measured repeatedly until consistency (2% tolerance in drift) was achieved or a maximum number of 10 repeats had been reached, as described elsewhere [28].

Impedance data were collected in a quasi-linear temperature mode (QL mode) in 1 °C steps over the temperature range 200 to 800 °C on cooling at a rate of 0.5 °C min^{-1}. Short scans over the frequency range 1×10^3 Hz to 1×10^4 Hz (range chosen to ensure capture of the total resistance, R_{total}, of the sample) were performed every 2 min.

The ionic and electronic components of total conductivity were determined using a modified EMF method. Pellets (*ca*. 17 mm in diameter and 2 mm in thickness with Pt electrodes of *ca*. 10 mm diameter) were measured in the concentration cell O_2($pO_2 = 1.01 \times 10^5$ Pa): Pt | sample | Pt : O_2 ($pO_2 = 0.2095 \times 10^5$ Pa) with an external adjustable voltage source, as previously described [29]. Measurements were performed on cooling in the approximate temperature range 800 °C to 500 °C.

Conductivity data were modelled on the basis of the “cube-root” model using self-made fitting procedures in the MATLAB software package. Details of the fitting procedures, including fitting scripts are included in the electronic supporting information of this paper.

3. Results and discussion

3.1 Structure – general description

The fitted X-ray diffraction profiles for $Bi_{0.75}Pr_{0.25}O_{1.5}$ at room temperature are shown in Fig. 1. A rhombohedral substructure model was used in the fit. This model does not account for the weak superstructure peaks evident in the neutron diffraction data, but is in good agreement with the structure presented by Drache *et al*. for β_2-$Bi_{0.775}Pr_{0.225}O_{1.5}$ [10]. While electron diffraction studies have identified a modulation vector in [-111] reciprocal lattice images of other rare earth substituted β_2-phases [15], full characterization of the superstructure has not been possible to date. The absence of the superlattice peaks in the X-

ray diffraction data suggest that they are associated with ordering on the oxide-ion sublattice. There is no evidence in the diffraction data for the monoclinic ε-phase found in the related Bi_2O_3-La_2O_3 system on annealing at around 300 °C [17].

The layered structure of the β_2 phase is shown in Fig. 2a. The structure consists of neutral $(M_3O_{4.5})_n$ layers, separated by a van der Waals gap of around 3.2 Å (a method for calculating the van der Waals gap is given in the supporting information). In the *R*-3*m* subcell model used in the refinement, two crystallographically distinct cation sites are located within the layers. The central 3*a* site at 0,0,0 is shared by both Bi^{3+} and Pr^{3+} cations, while the outer 6*c* site at 0,0,0.225 is exclusively occupied by Bi^{3+}. While the layers are fluorite like in nature, the van der Waals gap disrupts the cubic close-packed arrangement resulting in an ABCBCA type ordering.

Oxide ions are distributed over three crystallographically distinct sites in this structure. O(1) is located inside the layers, bonding the outer cations located on the 6*c* site to the central cations located on the 3*a* site. O(2) and O(3) sites , which are located at the edge of the layers, near the van der Waals gap, show partial occupancy. The concentration of intrinsic oxide-ion vacancies, at the edge of the fluorite like layers, is high with an estimated 37.5% of available O(2) and O(3) oxide ion sites being vacant at room temperature. Oxide ions on the O(2) site are bonded to cations on both the 3*a* and 6*c* sites, while oxide ions on the O(3) site are bonded to the outer cations only. At room temperature, there is no evidence for oxide ion scattering within the van der Waals gap. The 3*a* cations show a distorted cubic coordination, while the 6*c* cations show an average coordination number of 4.75, in a distorted pyramidal configuration. These cations have one bond to O(1) and 3 contacts each to partially occupied O(2) and O(3) sites. The large thermal parameter on O(3), as shown in Table 1, suggests significant positional disorder.

3.2 Crystal structure - thermal evolution

Fig. 3a shows details of the X-ray diffraction patterns of $Bi_{0.75}Pr_{0.25}O_{1.5}$ as a function of temperature on heating and cooling. There are no obvious changes in the diffraction pattern over the studied temperature range, confirming that the basic rhombohedral structure is maintained throughout. However, the thermal variation of unit cell volume (Fig. 3c), reveals a significant reversible step-like change in volume between 700 °C and 750 °C, consistent with the appearance of the β_1 phase at high temperatures [12]. This transition is of the order-disorder type, evidenced by a loss of superlattice ordering at high temperatures (Fig. 3b).

Interestingly, while the $\beta_2 \leftrightarrow \beta_1$ phase transition is clearly visible as a step in the thermal evolution of both *a*- and *c*- unit cell dimensions (Fig. 4a), in the case of the *c*-dimension, it is additionally preceded by non-linear behavior over the approximate temperature range 350 – 700 °C. The thermal evolution of the fluorite-like block dimension and the van der Waals gap in $Bi_{0.75}Pr_{0.25}O_{1.5}$ is shown in Fig. 4b. While the fluorite-like block size increases linearly over the studied temperature range, the van der Waals gap remains approximately constant up to *ca*. 500 °C. Above 500 °C, a gradual widening of the gap is observed with a threshold at *ca*. 700 – 750 °C, correlating with the temperature of the $\beta_2 \leftrightarrow \beta_1$ phase transition.

The refined structural parameters and significant contact distances for the studied compound at 25 and 800 °C are given in Tables 1 and 2, respectively. Unconstrained refinement of the structural model against the 800 °C data showed a deficiency in the oxide ion content, when the room temperature model was used. Fourier maps calculated from the neutron data at room temperature and at 800 °C are presented in Fig. 5. At 800 °C additional scattering is clearly evident from the atoms located in the van der Waals gap at around 0.175, 0.35, 0.5. When this site, denoted as O(4), was incorporated into the model, the site occupancy refinement accounted for the missing oxide-ion content and in the final refinement, the total oxide-ion content was fixed at the calculated value as presented in Table 1. While one cannot exclude the possibility of a small degree of oxidation of praseodymium to the 4+ oxidation state, the free refinement of the total oxide ion occupancy prior to the final refinement suggests that this is minimal, with a refined total of 13.51(*) oxygen atoms per unit cell. Furthermore, thermogravimetric studies suggest negligible mass change over the studied temperature range (Fig. S1). A schematic structure of the β_1 phase, including O(4) sites, is presented in Fig. 2b. It should be noted, that the coordinates of the O(4) oxide-ion site determined in the present work for $Bi_{0.75}Pr_{0.25}O_{1.5}$ are slightly different than those found by Obbade *et al*. in the structure of $Bi_{0.775}Pr_{0.225}O_{1.5}$ [15].

The thermal variation of the refined fractional occupancy of the O(4) site is shown in Fig. 6. A value close to zero is observed for temperatures from ambient up to *ca*. 500 °C. At higher temperatures, the O(4) site occupancy gradually increases and at *ca.* 750 °C a step change in occupancy occurs. This variation reflects those seen for the *c*-axis dimension and the van der Waals gap size with temperature (Fig. 4), indicating that the observed expansion of the van der Waals gap is induced by the appearance of interstitial oxide ions within the gap space. The refined O(4) site occupancy reaches a value of 0.035(3) at 800 °C, corresponding to 0.63(5) interstitial oxide ions per unit cell.

3.3 Ionic conductivity

The Arrhenius plot of total conductivity for $Bi_{0.75}Pr_{0.25}O_{1.5}$ is presented in Fig. 7. The plot is reproducible over heating and cooling cycles, with a step change in total conductivity clearly evident at *ca*. 730 °C, associated with the $\beta_2 \leftrightarrow \beta_1$ phase transition observed in the structural data. Even though the conductivity change seems to be sharp and step-like, close examination of data collected with using a narrower temperature interval (presented in the supplementary information, Fig. S2) reveals a more continuous nature for this transition.

Below *ca*. 400 °C, linear type behaviour is observed with a corresponding activation energy of ΔE_{LT} = 0.913(1) eV. In the intermediate temperature range (*ca*. 450 °C to 700 °C), non-linearity in the Arrhenius plot is seen. Owing to experimental limitations, conductivity above the phase transition was only measured over a very short temperature range, and consequently the linearity of the Arrhenius plot in this region, as well as the value of activation energy of conductivity, were determined with significant uncertainty. The activation energy of conductivity in the high temperature β_1 phase (ΔE_{HT}) was estimated as 0.739(7) eV.

The deviation from linearity in the Arrhenius plot between *ca*. 450 °C to 700 °C, together with the step change in total conductivity at *ca*. 730 °C, reflects the thermal variation in the *c*-axis dimension, which is predominantly due to increases in the size of the van der Waals gap (Fig. 4), caused by migration of oxygen ions into the interstitial O(4) sites (Fig . 6). Thus, a clear correlation between structural and electrical properties is evident.

3.4 Transference numbers

$Bi_{0.75}Pr_{0.25}O_{1.5}$ exhibits ionic transference numbers of 0.9 to 1.0 over the temperature range *ca.* 500 – 800 °C (Fig. 8a), typical for the rhombohedral phase [9]. The step change seen in total conductivity at the $\beta_2 \leftrightarrow \beta_1$ phase transition is mostly due to the ionic component; however, some change in the electronic component is also observed at *ca*. 730 °C (Fig. 8b). The predominance of ionic conductivity in $Bi_{0.75}Pr_{0.25}O_{1.5}$ allows the electronic component of total conductivity to be neglected in further analysis.

3.5 Conductivity pathways and modelling of conductivity data

At room temperature the oxide ion sublattice in $Bi_{0.75}Pr_{0.25}O_{1.5}$ was modelled using three oxygen sites O(1), O(2) and O(3) in the *R*-3*m* subcell model. The O(1) site remained

fully occupied over the whole studied temperature range and is strongly bonded to Bi/Pr(1) cations inside the fluorite-like block. They are therefore unlikely to participate in oxide ion migration. However, at the edge of the fluorite like block, significant local disorder in the oxide ion sublattice is observed even at room temperature, as manifested by partial occupation of O(2) and O(3) sites (Table 1). The excess of available oxide ion sites, i.e. high oxide ion vacancy concentration, together with short O(2)…O(3) distances provides conditions suitable for high oxide ion mobility. The conduction pathway *via* O(2) and O(3) sites is 2-dimesional in nature, being restricted to the edge of the fluorite like blocks and hence is described here as the intra-planar pathway. A schematic representation of this pathway is presented in Fig. 9a.

At higher temperatures, approaching the phase transition temperature, occupation of an additional interstitial site, O(4), located in the van der Waals gap, is observed. This suggests oxide ion transport between adjacent fluorite-like blocks and therefore is described here as inter-planar as represented schematically in Fig 9b. It should be noted that even though the inter-planar conduction pathway facilitates oxide-ion motion between adjacent blocks, the non-participation of the O(1) sites in conduction means that they act as a barrier to conduction, making the inter-planar pathway essentially 2-dimensional in nature.

Mercurio *et al*. [30] also considered these two pathways for ion transport in rhombohedral $Bi_{0.7}La_{0.3}O_{1.5}$. However, while they considered the interstitial O(4) to be important for oxide ion transport, they argued, that the motion of oxide ions at the edges of the fluorite-like blocks (i.e. O(2) to O(3) sites) is mainly responsible for the step change in ionic conductivity. Ahi *et al*. [11] also argued that inter-planar pathways provide a negligible contribution to conductivity, due to the low occupancy of the O(4) interstitial sites in rhombohedral $Bi_{0.775}La_{0.225}O_{1.5}$. However, in the present work, our results suggest that the contribution of the inter-planar pathway is more significant. The O(4) site occupancy changes rapidly with temperature in the vicinity of the $\beta_2 \leftrightarrow \beta_1$ phase transition (Fig. 6) and it is considered here that inter-planar conduction *via* the O(4) interstitials is responsible for both the non-linearity of total conductivity above *ca*. 450 °C and the step change in conductivity at the $\beta_2 \leftrightarrow \beta_1$ phase transition.

In the present work, both conduction pathways were considered during the fitting procedure. Although an increase in O(4) occupancy must result in a deficiency of oxide ions in the O(2) and/or O(3) sites and thus there is a relationship between the inter-planar and intra-planar conduction processes, in the analysis it was assumed, that these components are independent. Consequently, the total ionic conductivity of $Bi_{0.75}Pr_{0.25}O_{1.5}$ is considered to be the simple sum of intra-planar and inter-planar conductivities.

$$\sigma_{\mathrm{i}} \approx \sigma_{\mathrm{intra-planar}} + \sigma_{\mathrm{inter-planar}} \quad (1).$$

Intra-planar conductivity ($\sigma_{\mathrm{intra\text{-}planar}}$) is governed by the hopping mechanism and can be modelled with a classical Arrhenius dependence:

$$\sigma_{\mathrm{intra-planar}} = \frac{zq}{V}\frac{\sigma_0}{T}\exp\left(-\frac{H_{\mathrm{m1}}}{kT}\right) \quad (2)$$

where the product zq is charge, V is the unit cell volume, σ_0 is a pre-exponential factor which contains such quantities as migration entropy, concentration of mobile ionic carriers, jump distance and attempt frequency, and H_{m1} is the migration enthalpy for the intra-planar migration path.

The inter-planar conductivity is associated with O(4) interstitial sites, the occupancy of which increases rapidly in the vicinity of the $\beta_2 \leftrightarrow \beta_1$ phase transition. The "cube-root" model has proved to be successful in modelling conductivity in systems where the concentration of defects changes in a cascade manner [24] and therefore in the present work modification of the "cube-root" model was applied for modelling of the inter-planar conductivity [25]. In general in the cube root model, a term responsible for lowering the energy of defect formation is included. In this case, defect concentration per unit cell can be expressed as:

$$\frac{c}{(1-c)} = \exp\left(-\frac{H_{\mathrm{f}} - T\Delta S_{\mathrm{f0}} - Jc^{1/n}}{2kT}\right) \quad (3)$$

where c denotes defect concentration per unit cell, H_{f} is the enthalpy of point defect formation (presumed to be anion Frenkel defects), ΔS_{f0} is the change in vibrational entropy associated with defect formation, J is related to the electrostatic interaction between defects and n is the degree of the root term reflecting the dimensionality of conductivity (e.g. n = 3 for classical 3-dimensional ionic conductors). In principle, the Gibbs enthalpy of defect formation here is modified by the product of the n^{th} root of defect concentration per unit cell and the J parameter [31]. This approach allows for the modelling of the non-linear behaviour in the vicinity of the phase transition.

To avoid increase in defect concentration *ad infinitum*, the (1 - c) expression is added to the denominator in Eq. (3). This expression describes site availability in the

crystallographic structure for next-nearest defects. Here it is presented in a simplified form; in some cases however it is necessary to include site restrictions specific to a particular crystal structure. In fact, such corrections are necessary in the case of $Bi_{0.75}Pr_{0.25}O_{1.5}$. Considerations relating to site restrictions in the rhombohedral structure of $Bi_{0.75}Pr_{0.25}O_{1.5}$ are discussed in the supplementary information.

Inter-planar mobility, $\mu_{\mathrm{inter-planar}}$, is thermally activated with H_{m2} being the migration enthalpy of the inter-planar migration process:

$$\mu_{\mathrm{inter-planar}} = \frac{\mu_{\mathrm{o}}}{T} 2(1-c) \exp\left(-\frac{H_{\mathrm{m2}}}{kT}\right) \quad (4)$$

μ_0 in principle contains the same quantities as σ_0 from Eq. (2), except for the concentration of mobile ionic carriers, which in this case is denoted by Eq. (3). Also, μ_0 and σ_0 are associated with two different migration processes. As for high defect concentrations, the mobility may be limited by the number of available sites and Eq. (4) has to be corrected by a (1 - *c*) expression [25].

The total ionic conductivity is a product of Eq. (3), (4) and charge:

$$\sigma_{\mathrm{inter-planar}} = \frac{zq}{V} \exp\left(-\frac{H_{\mathrm{f}} - T\Delta S_{\mathrm{f0}} - Jc^{1/n}}{2kT}\right) \frac{\mu_{\mathrm{o}}}{T} 2(1-c)^2 \exp\left(-\frac{H_{\mathrm{m2}}}{kT}\right) \quad (5)$$

Conductivity data were modelled as a combination of inter-planar and intra-planar components. However, to improve accuracy of fitting, impedance data for $Bi_{0.75}Pr_{0.25}O_{1.5}$ were additionally collected in quasi-linear (QL) temperature mode in 1 °C steps. The obtained QL conductivity as well as the fitted inter-planar and intra-planar components are shown in Fig. 10a. The combination of inter-planar and intra-planar conductivities results in a very good fit to the QL conductivity data, with a low mean squared error (MSE) value. The refined parameters are given in Table 3, with values of constant parameters given in Table S2 in the supplementary information. The H_{m1} parameter (intra-planar migration enthalpy) is in good agreement with the low temperature activation energy (ΔE_{LT} = 0.913(1) eV), indicating the dominance of intra-planar conductivity at lower temperatures. The inter-planar pathway starts to play a more significant role above *ca.* 500 °C. This temperature correlates with the temperature of the appearance of oxide ions in the O(4) site. The inter-planar contribution is required to accurately model the non-linear pre-transition behaviour as well as the conductivity above the phase transition. The high temperature activation energy (ΔE_{HT} =

0.739(7) eV) lies between the refined values for inter-planar and intra-planar migration enthalpies (0.4807(2) and 0.9043(1) eV, respectively), which suggests, that the measured QL conductivity is influenced by both inter-planar and intra-planar conductivities. Indeed, extrapolation of the modelled curves to higher temperatures (as shown in Fig. 10a) shows that the conductivity above the phase transition is a resultant of both inter- and intra-planar migration processes.

The refined thermodynamic parameters H_f, S_{f0} and J (Table 3) can be used to characterise the thermal evolution of defect concentration per unit cell, c (Eq. 4). The Arrhenius type plot of defect concentration (Fig. 10b) shows a step change at *ca*. 730 °C confirming, that the $\beta_2 \leftrightarrow \beta_1$ phase transition is correlated with defect concentration changes and occurs at a critical value of defect concentration [23].

The nature of the phase transition can be determined using the ratio of two parameters from the "cube-root" model, γ and γ_{crit} [25], where:

$$\gamma = J/H_f \tag{6}$$

and

$$\gamma_{crit} = \frac{(n+1)^{1/n}}{1+\frac{1}{n+1}\left(\ln n+\frac{\Delta S_{f,0}}{2k}\right)} \tag{7}$$

In the present work $\gamma < \gamma_{crit}$, (Table 3), corresponding to a diffuse phase transition, rather than the abrupt structural change that occurs in a first order transition. This is in good agreement with the structural and electrical results, where as discussed above, the phase transition appears more continuous in nature.

The dimensionality of conductivity can be examined through refinement of the value of n, which in the present case refined to a value of 2.333(2), consistent with predominantly 2-dimensional conduction.

It should be noted, that non-linearity in the Arrhenius type plot of total conductivity for $Bi_{0.75}Pr_{0.25}O_{1.5}$ could be related not only to changes in concentration of oxide-ion vacancies (intra-planar pathway) or interstitial oxide-ions (inter-planar pathway), but also with variation of charge carrier mobility. The volume expansion affects the energy landscape and could result in a lowering of energy barriers for oxide-ion hopping between sites, resulting in increased ion mobility. In the present work, the thermal variation of unit cell

volume reveals a significant reversible step-like change between 700 °C and 750 °C (Fig. 3c) and therefore the influence of volume changes on ion mobility should be considered. Following the approach of Schmalzried [32], volume correction terms (H_m, H_f or J parameters linearly proportional to the volume change) were introduced for both intra- and inter-planar conductivity formulae. Interestingly, this approach results in only minimal change to the overall fit quality, suggesting that defect concentration changes dominate electrical performance in the studied system. Details of these fits are given in the supporting information.

It is well established for the bismuth based rhombohedral phases that decreasing lanthanide metal dopant ionic radius, results in an increase of phase transition temperature up to the point, where the cubic δ-phase is more stable than the rhombohedral β_1-phase [33]. If indeed the phase transition temperature for the rhombohedral phase is determined by a critical value of interstitial oxide-ion concentration in the van der Waals gap, then this would suggest a causal relation between average cation size in the mixed cation layer and the thermal evolution of defect concentration. It is expected that the ionic radius of the lanthanide dopant will have an impact on lattice parameters, especially the fluorite-like block and van der Waals gap size. Consequently this might influence the migration of oxide ions into the van der Waals gap. If this is the case, then manipulation of lattice size by doping would be reflected in the thermodynamic parameters discussed above.

4. Conclusions

$Bi_{0.75}Pr_{0.25}O_{1.5}$ exhibits a β_2 rhombohedral type structure at room temperature. On heating, above *ca.* 500 °C, occupation of interstitial oxygen sites in the van der Waals gap between the fluorite like blocks of the layered structure is observed. At higher temperatures, between 700 - 750 °C, further increase in the fractional occupancy of the O(4) interstitial site correlates with a widening of the van der Waals gap and an increase in unit cell volume. These structural changes are correlated with the observed $\beta_2 \leftrightarrow \beta_1$ phase transition.

The conductivity of $Bi_{0.75}Pr_{0.25}O_{1.5}$ is high (~0.5 S cm^{-1} at 800 °C) and predominantly ionic, with oxide-ion transference numbers above 0.9, over the temperature range 500-800 °C. A step change in ionic conductivity observed at *ca.* 730 °C is associated with the $\beta_2 \leftrightarrow \beta_1$ phase transition. Conductivity data have been modeled using a modification of the “cube root” model, with ionic conductivity as the result of contributions from two main pathways. At low temperature, ionic conductivity appears predominantly within the fluorite-like blocks

(intra-planar pathway) and shows classical Arrhenius behavior. At intermediate temperatures (above *ca.* 500 °C), conductivity via interstitial sites in the van der Waals gap (inter-planar pathway) begins to play a more significant role. Thus it appears that the process of oxide-ion migration from the fluorite-like blocks to the van der Waals gap space is mostly responsible for the step change in ionic conductivity as well as the $\beta_2 \leftrightarrow \beta_1$ phase transition itself.

Refinement of the degree of the root in the "cube root" model indicates conductivity to be predominantly 2-dimensional, consistent with previous single crystal studies. The study therefore shows the applicability of this relatively simple model to systems that show lower dimensions of conduction than classical 3-dimensional conductors.

Acknowledgements

This work has been supported by the National Science Centre, Poland grant number UMO-2018/31/B/ST5/03161. We are grateful to Dr Rotraut Merkle at Max-Planck Institute for Solid State Research, Stuttgart for a fruitful discussion on the "cube-root" model. We gratefully acknowledge the STFC ISIS facility at the Rutherford Appleton Laboratory for neutron beam time (Award Number: RB 920184) and Dr Ron Smith at the ISIS facility for his help in data collection.

References

[1] H.A. Harwig, A.G. Gerards, J. Solid State Chem. 26 (1978) 265–274.

[2] T. Takahashi, T. Esaka, H. Iwahara, J. Appl. Electrochem. 5 (1975) 197–202.

[3] T. Takahashi, H. Iwahara, T. Arao, J. Appl. Electrochem. 5 (1975) 187–195.

[4] T. Takahashi, H. Iwahara, Y. Nagai, J. Appl. Electrochem. 2 (1972) 97–104.

[5] P.D. Battle, C.R.A. Catlow, L.M. Moroney, J. Solid State Chem. 67 (1987) 42–50.

[6] P.D. Battle, C.R. a. Catlow, a. V. Chadwick, P. Cox, G.N. Greaves, L.M. Moroney, J. Solid State Chem. 69 (1987) 230–239.

[7] N. Jiang, E.D. Wachsman, J. Am. Ceram. Soc. 82 (1999) 3057–3064.

[8] P. Conflant, J.C. Boivin, D. Thomas, J. Solid State Chem. 35 (1980) 192–199.

[9] T. Esaka, H. Iwahara, H. Kunieda, J. Appl. Electrochem. 12 (1982) 235–240.

[10] M. Drache, S. Obbade, J.P. Wignacourt, P. Conflant, 359 (1999) 349–359.

[11] A. Ahi, A. Mellergård, S.G. Eriksson, Solid State Ionics. 177 (2006) 289–297.

[12] P. Conflant, C. Follet-Houttemane, M. Drache, J. Mater. Chem. 1 (1991) 649–653.

[13] M. Drache, J.P. Wignacourt, P. Conflant, J. Solid State Chem. 149 (2000) 341–348.

[14] M. Drache, M. Huve, P. Roussel, P. Conflant, Mater. Res. Bull. 38 (2003) 113–124.

[15] S. Obbade, M. Huve, E. Suard, M. Drache, P. Conflant, J. Solid State Chem. 168 (2002) 91–99.

[16] D. Mercurio, J.C. Champarnaud-Mesjard, B. Frit, P. Conflant, J.C. Boivin, T. Vogt, J. Solid State Chem. 112 (1994) 1–8.

[17] M. Drache, J.P. Wignacourt, P. Conflant, J. Solid State Chem. 151 (2000) 281–285.

[18] M. Drache, P. Roussel, J.P. Wignacourt, Chem. Rev. 107 (2007) 80–96.

[19] J.C. Boivin, D. Thomas, Solid State Ionics. 5 (1981) 523–526.

[20] T. Kurosawa, J. Phys. Soc. Japan. 12 (1957) 338–346.

[21] B.A. Huberman, Phys. Rev. Lett. 32 (1974) 1000–1002.

[22] M.J. Rice, S. Strassler, G.A. Toombs, Phys. Rev. Lett. 32 (1974) 596–599.

[23] J. Maier, W. Münch, Zeitschrift Fur Anorg. Und Allg. Chemie. 626 (2000) 264–269.

[24] N. Hainovsky, J. Maier, Radiat. Eff. Defects Solids. 137 (1995) 267–271.

[25] N. Hainovsky, J. Maier, Phys. Rev. B. 51 (1995) 199–205.

[26] A.C. Larson, R.B. Von Dreele, L. Alamos, Los Alamos Natl. Lab. Rep. (1987).

[27] K. Momma, F. Izumi, J. Appl. Crystallogr. 44 (2011) 1272–1276.

[28] J.R. Dygas, P. Kurek, M.W. Breiter, Electrochim. Acta. 40 (1995) 1545–1550.

[29] M. Malys, J.R. Dygas, M. Holdynski, A. Borowska-Centkowska, W. Wrobel, M. Marzantowicz, Solid State Ionics. 225 (2012) 493–497.

[30] D. Mercurio, M. El Farissi, J.C. Champarnaud-Mesjard, B. Frit, P. Conflant, G. Roult, J. Solid State Chem. 80 (1989) 133–143.

[31] F. Zimmer, P. Ballone, J. Maier, M. Parrinello, Berichte Der Bunsen-Gesellschaft-Physical Chem. Chem. Phys. 101 (1997) 1333–1338.

[32] H. Schmalzried, Zeitschrift Fur Phys. Chemie Neue Folge. 22 (1959) 199–208.

[33] J.C. Boivin, G. Mairesse, Chem. Mater. 10 (1998) 2870–2888.

Figures

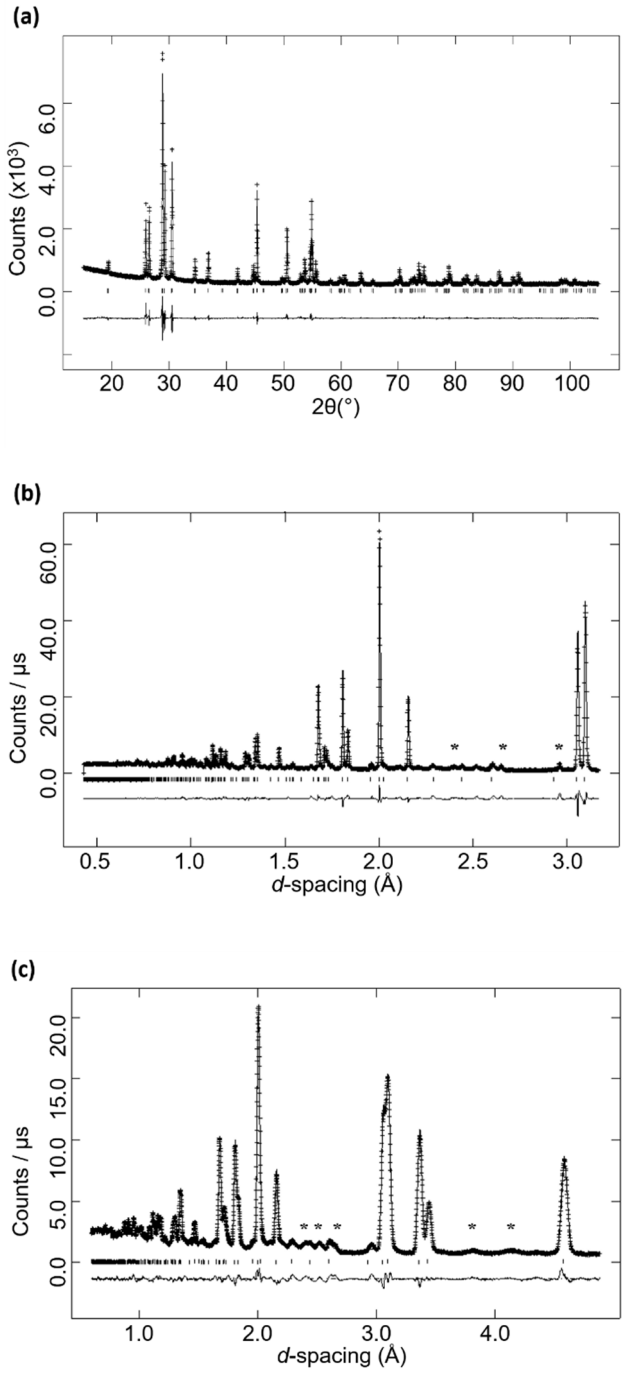

Fig. 1.

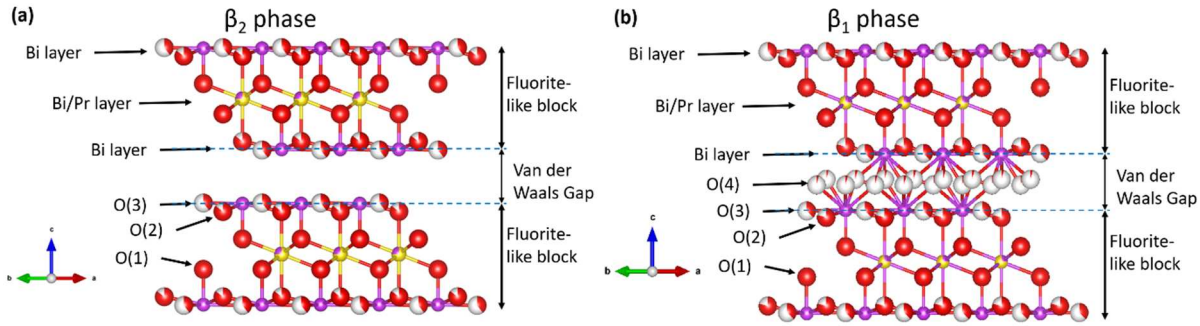

Fig. 2.

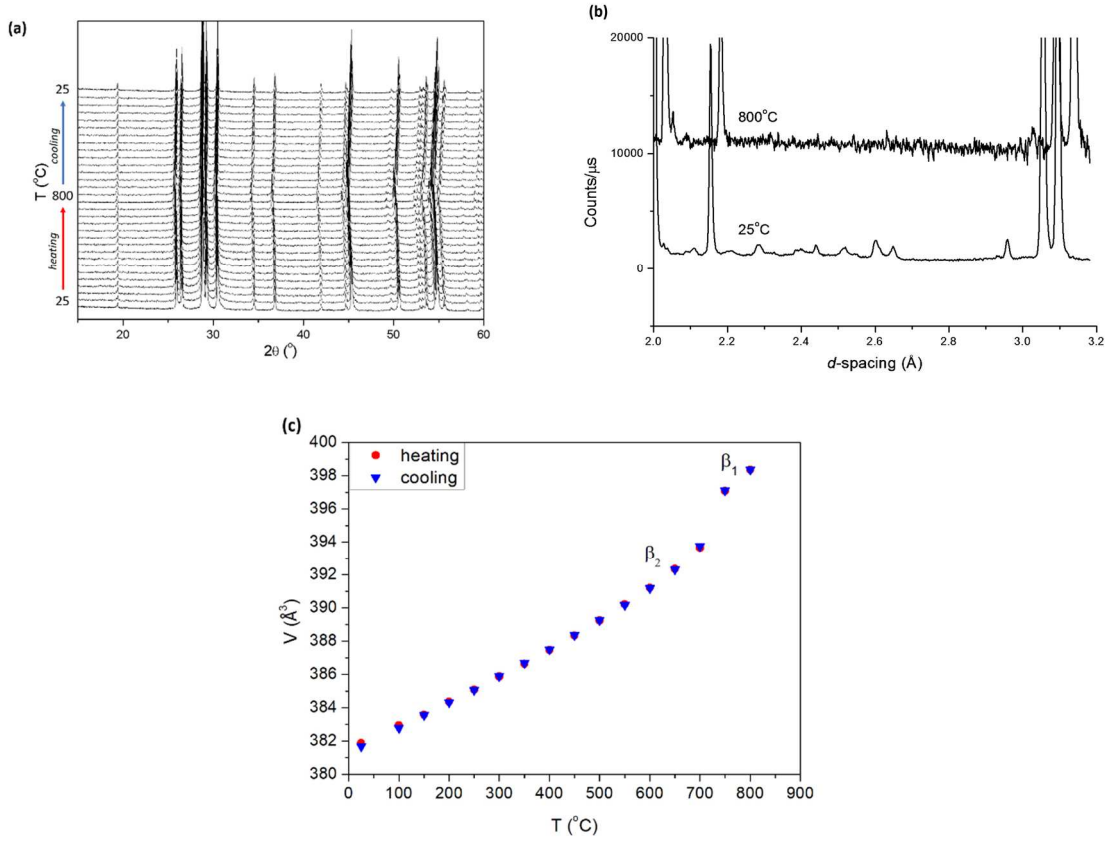

Fig. 3.

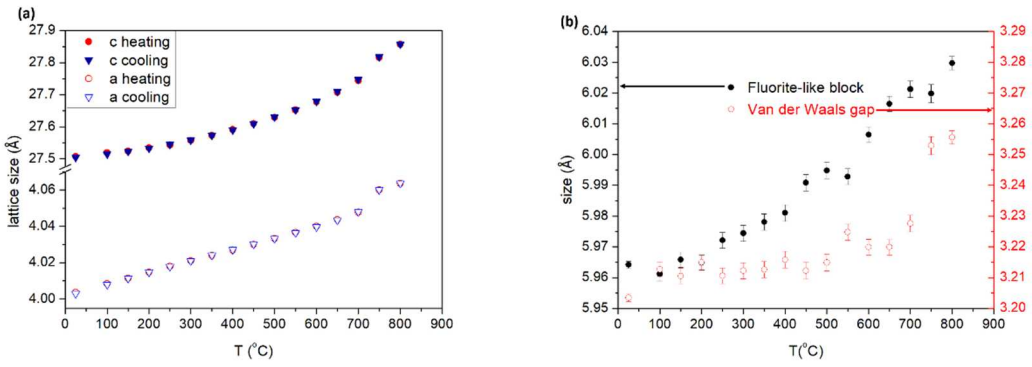

Fig. 4.

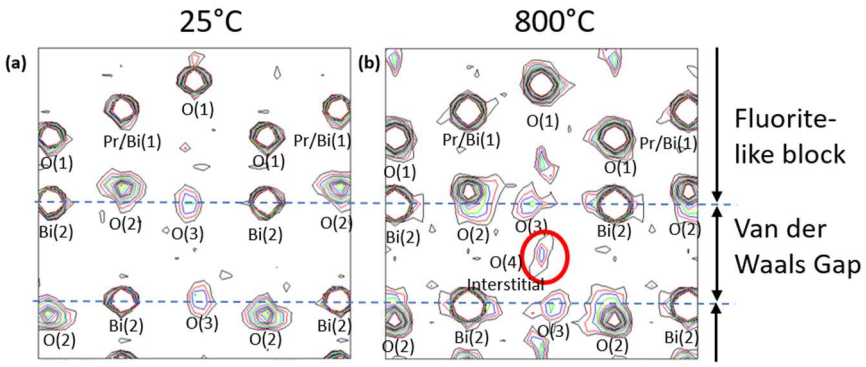

Fig. 5.

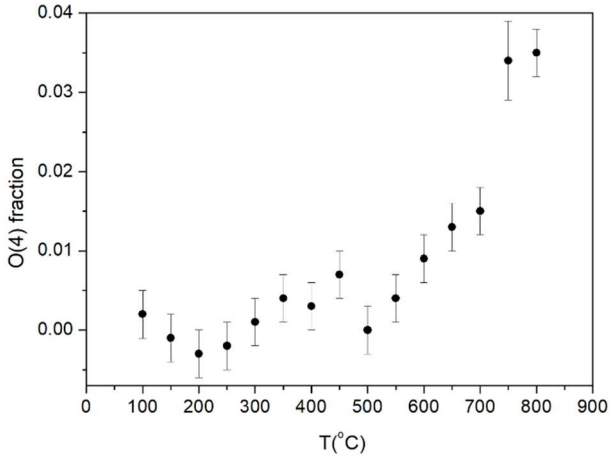

Fig. 6.

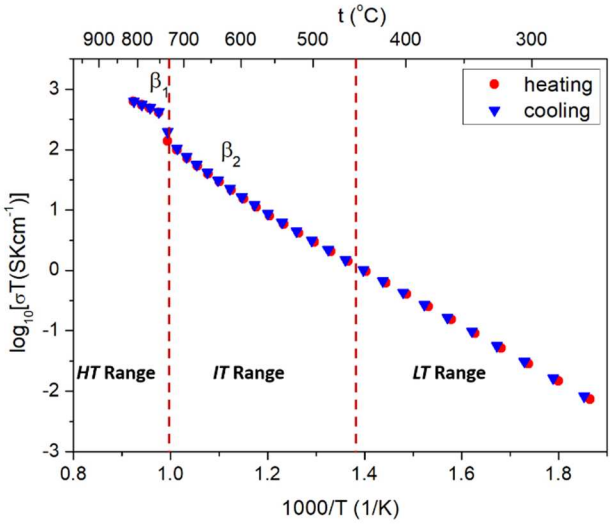

Fig. 7.

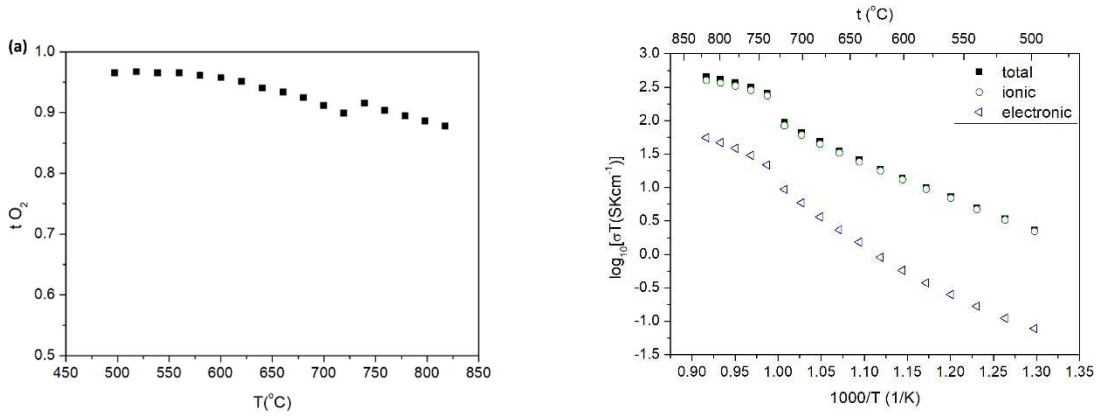

Fig. 8.

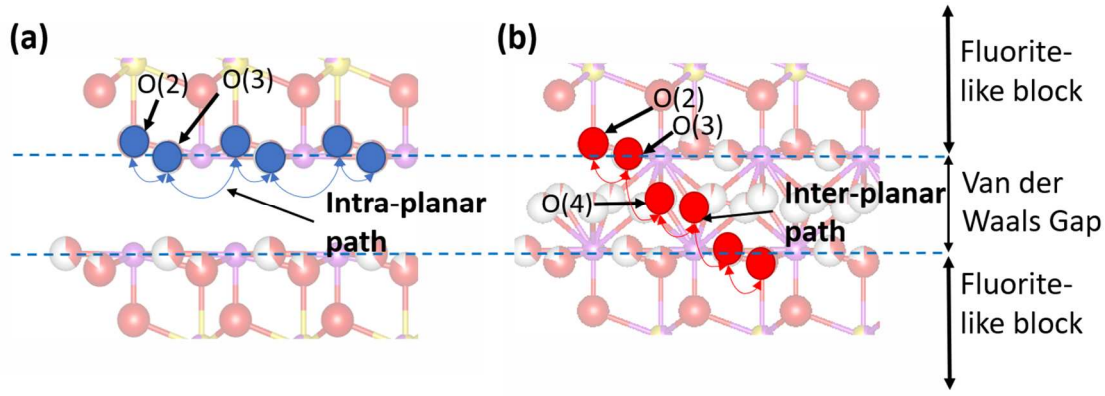

Fig. 9.

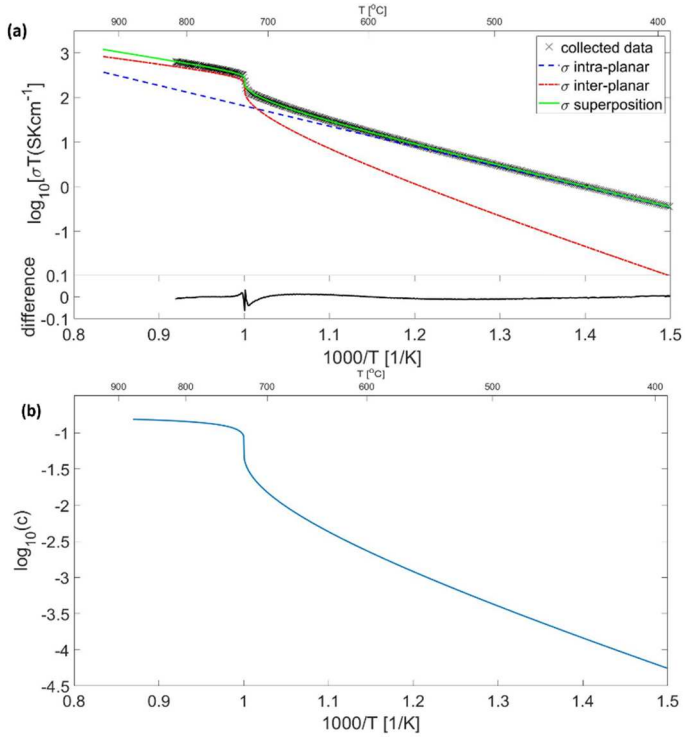

Fig. 10.

Tables

Table 1. Refined structural parameters for $Bi_{0.75}Pr_{0.25}O_{1.5}$ at (a) 25 °C (subcell model) and (b) 800 °C. Estimated standard deviations are given in parentheses

(a) 25 °C (β_2 phase)								
Atom	**site**	**x**	**y**	**z**	**Occ.**	**U_{11}=U_{22} (Å^2)[a]**	**U_{33} (Å^2)**	**U_{13} (Å^2)**
Bi/Pr(1)	**3a**	**0.0**	**0.0**	**0.0**	**0.25/0.75**	**0.0133(4)**	**0.0375(8)**	**0.0066(2)**
Bi(2)	**6c**	**0.0**	**0.0**	**0.22491(2)**	**1**	**0.0250(3)**	**0.0108(3)**	**0.0126(2)**
O(1)	**6c**	**0.0**	**0.0**	**0.30075(4)**	**1**	**0.0279(4)**	**0.0200(5)**	**0.0140(2)**
O(2)	**6c**	**0.0**	**0.0**	**0.09147(6)**	**0.838(4)**	**0.096(1)**	**0.0246(8)**	**0.048(1)**
O(3)	**6c**	**0.0**	**0.0**	**0.44304(2)**	**0.412(4)**	**0.154(4)**	**0.047(3)**	**0.077(2)**
(b) 800 °C (β_1 phase)								
atom	**site**	**x**	**y**	**z**	**Occ.**	**U_{11}= U_{22} (Å^2)[a]**	**U_{33} (Å^2)**	**U_{13} (Å^2)**
Bi/Pr(1)	**3a**	**0.0**	**0.0**	**0.0**	**0.25/0.75**	**0.0351(11)**	**0.0592(19)**	**0.0176(6)**
Bi(2)	**6c**	**0.0**	**0.0**	**0.22510(4)**	**1**	**0.0516(7)**	**0.0315(8)**	**0.0258(4)**
O(1)	**6c**	**0.0**	**0.0**	**0.30138(10)**	**1**	**0.0576(15)**	**0.0562(19)**	**0.0288(8)**
O(2)	**6c**	**0.0**	**0.0**	**0.0929(2)**	**0.803(9)**	**0.137(4)**	**0.0703(36)**	**0.069(2)**
O(3)	**6c**	**0.0**	**0.0**	**0.43918(70)**	**0.342(9)**	**0.098(9)**	**0.258(17)**	**0.049(5)**
O(4)	**18h**	**0.1645(53)**	**0.329(11)**	**0.5083(17)**	**0.035(3)**	**0.085(24)**	**-**	**-**

[a] $U_{13} = U_{23} = 0$. In the case of O(4) only U_{iso} was refined.

Table 2. Significant contact distances in $Bi_{0.75}Pr_{0.25}O_{1.5}$ at 25 °C and 800 °C. Estimated standard deviations are given in parentheses

	Contact distance (Å)	
Bond	**25 °C (β_2 phase)**	**800 °C (β_1 phase)**
Bi/Pr(1)-O(1)	**2.4794(4)**	**2.5098(10)**
Bi/Pr(1)-O(2)	**2.5158(15)**	**2.589(4)**
Bi(2)-O(1)	**2.0858(12)**	**2.1248(30)**
Bi(2)-O(2)	**2.3583(3)**	**2.3851(8)**
Bi(2)-O(3)	**2.3121(1)**	**2.3476(5)**
Bi(2)-O(4)	**-**	**2.4646(6)** **2.2105(9)**

Table 3. Fitting parameters for QL conductvity data for $Bi_{0.75}Pr_{0.25}O_{1.5}$. ΔS_f here is expressed as a product of the Boltzmann constant.

Parameter	Value
H_{m1} [eV]	0.9043(1)
σ_0 [S K cm^2 C^{-1}]	373.2(4)
H_f [eV]	1.5055(5)
ΔS_{f0} /k	5.781(5)
J [eV]	1.775(1)
H_{m2} [eV]	0.4807(2)
μ_0 [S K cm^2 C^{-1}]	103.1(3)
n	2.333(2)
γ	1.179
γ_{crit}	1.340
MSE	8.03×10^{-5}

Figure captions

Fig. 11. Fitted (a) X-ray, (b) neutron back scattering and (c) neutron low angle diffraction profiles for $Bi_{0.75}Pr_{0.25}O_{1.5}$ at 25 °C using the *R*-3*m* subcell model. Observed (+ symbols), calculated (line) and difference (lower) profiles are shown. Reflection positions are indicated by markers and asterisks (*) indicate superstructure peaks.

Fig. 12. Structure of $Bi_{0.75}Pr_{0.25}O_{1.5}$ (a) low temperature β_2 phase and (b) high temperature β_1 phase. Violet, yellow, red and white spheres represent Bi, Pr, O ions and O vacancies, respectively.

Fig. 13. (a) Thermal dependence of X-ray diffraction patterns, (b) neutron diffraction patterns at 25 °C and 800 °C and (c) thermal evolution of unit (sub)cell volume for $Bi_{0.75}Pr_{0.25}O_{1.5}$.

Fig. 14. Thermal evolution of (a) *a*- and *c*- lattice parameters and (b) fluorite-like block dimension and van der Waals gap size for $Bi_{0.75}Pr_{0.25}O_{1.5}$.

Fig. 15. Fourier maps (F_{obs}) from neutron diffraction data for $Bi_{0.75}Pr_{0.25}O_{1.5}$ at (a) 25 °C and (b) 800 °C. The red circle in (b) indicates the position of O(4).

Fig. 16. Thermal variation of O(4) fractional site occupancy for $Bi_{0.75}Pr_{0.25}O_{1.5}$.

Fig. 17. Arrhenius plot of total conductivity for $Bi_{0.75}Pr_{0.25}O_{1.5}$. Dashed lines separate high (HT), intermediate (IT) and low (LT) temperature regions.

Fig. 18. Thermal variation of (a) ionic transference number and (b) electronic and ionic components of total conductivity for $Bi_{0.75}Pr_{0.25}O_{1.5}$. Data collected on cooling.

Fig. 19. Schematic representation of (a) intra-planar and (b) inter-planar conduction pathways.

Fig. 20. (a) Fitted QL conductivity data showing intra-planar and inter-planar components and difference (bottom) and (b) Arrhenius type plot of defect concentration per unit cell obtained from the “cube-root” model for $Bi_{0.75}Pr_{0.25}O_{1.5}$.

Supplementary Information

The influence of defect structure changes at phase transition on electrical properties in the $Bi_{0.75}Pr_{0.25}O_{1.5}$ oxide ion conductor

J. Jamroz,[1] M. Malys,[1] F. Krok,[1] J. Maier,[2] A. Kyriacou,[3] S. J. Ahmed,[3] I. Abrahams,[3*] W. Wrobel[1*]

[1]Faculty of Physics, Warsaw University of Technology, Koszykowa75, 00-662 Warszawa, Poland.

[2]Max Planck Institute for Solid State Research, 70569 Stuttgart, Germany

[3]Materials Research Institute, School of Biological and Chemical Sciences, Queen Mary University of London, Mile End Road, London E1 4NS, U.K.

Corresponding authors:

i.abrahams@qmul.ac.uk

wojciech.wrobel@pw.edu.pl

Table S1. Crystal and Refinement parameters for $Bi_{0.75}Pr_{0.25}O_{1.5}$ at room temperature and at 800 °C. Estimated standard deviations are given in parentheses.

Temperature	25 °C (β_2 phase) subcell model	800 °C (β_1 phase)
Chemical formula	$Bi_{0.75}Pr_{0.25}O_{1.5}$	$Bi_{0.75}Pr_{0.25}O_{1.5}$
Formula weight (g mol^{-1})	215.96	215.96
Crystal system	Rhombohedral	Rhombohedral
Space group	*R*-3*m*	*R*-3*m*
Unit cell dimensions (Å)	*a* = 4.0042(1)	*a* = 4.06455(4)
	c = 27.5030(9)	*c* = 27.8460(3)
Volume ($Å^3$)	381.90(3)	398.54(1)
Density (g cm^{-3})	8.451	8.098
Sample description	Yellow powder	Yellow powder
R-factors	Neutron (back-scattering)	Neutron (back-scattering)
	R_{wp}=0.0365 , R_p=0.0597	R_{wp}=0.0089 , R_p=0.0218
	Neutron (low-angle)	Neutron (low-angle)
	R_{wp}=0.0555 , R_p=0.044	R_{wp}=0.024 , R_p=0.0215
	X-ray	X-ray
	R_{wp}=0.0924 , R_p=0.0686	R_{wp}=0.0861 , R_p=0.0664
	Totals	Totals
	R_{wp}=0.0404 , R_p=0.0682	R_{wp}=0.0163 , R_p=0.064
	χ^2=12.64	χ^2=1.888

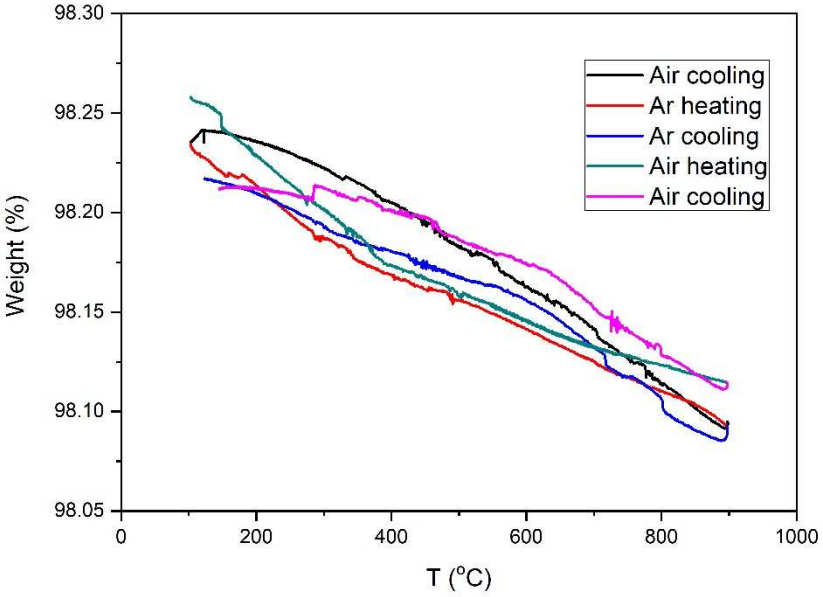

Fig. S1. TGA thermogram for $Bi_{0.75}Pr_{0.25}O_{1.5}$ showing cooling in air (black), heating under Ar (red), cooling under Ar (blue), heating in air (cyan) and cooling in air (pink). Data were collected using a TA instruments Q600 scanning differential thermal analyser at a heating/cooling rate of 10 ℃ min^{-1} in sequentially in flowing air, Ar and air.

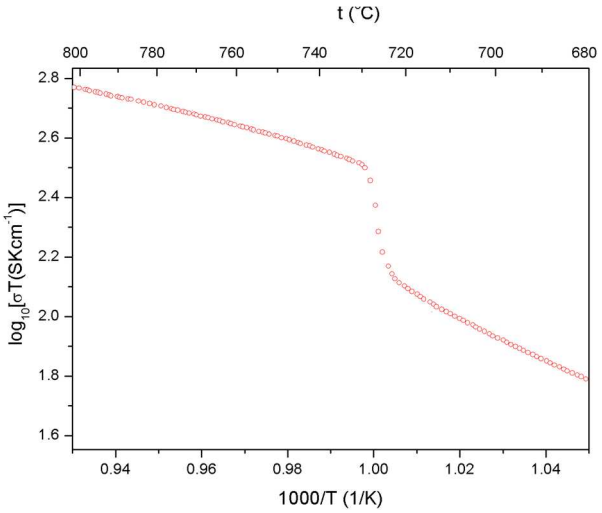

Fig. S2. Arrhenius plot of total conductivity for $Bi_{0.75}Pr_{0.25}O_{1.5}$ collected in quasi-linear temperature mode

Method to calculate the size of the van der Waals gap in the *R*-3*m* structure of $Bi_{0.75}Pr_{0.25}O_{1.5}$

Let *L* be the thickness of a layer and *G* be the height of the van der Waals gap (Fig. S3). One unit cell contains 3 layers and 3 gaps i.e. $c = 3L+3G$. The Bi(2)-Bi(2) distance along the *c*-axis is equivalent to 2 layers and 1 gap i.e. $d\{Bi(2)\text{-}Bi(2)\} = 2L + 1G$. The size of *L* and *G* can then be readily calculated through simultaneous equations.

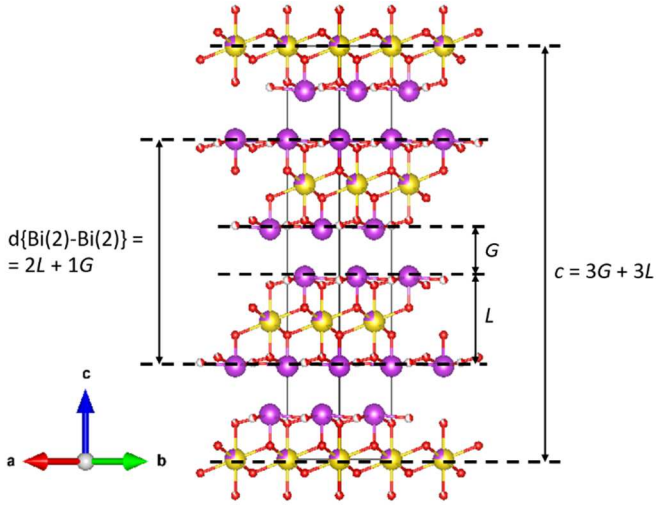

Fig. S3. Schematic representation of thickness calculation of fluorite-like layer and van der Waals Gap, marked as L and G respectively.

Site restriction considerations and values of the constants in the "cube-root" model

The expression (1 - *c*) from Eq. (3-5), which denotes the site restrictions of the crystal structure, can be described by a general formula of $\sqrt{g_i g_v(\alpha_i - c)(\alpha_v - c)}$. After [25], α_i and α_v denote occupiable crystallographic sites for interstitials and vacancies, respectively and g denotes the degeneracy of the sites. Thus, the product $g\alpha$ is the number of available sites for the first created defect (if all g's and α's have values equal to 1, the equation simplifies to (1-*c*)). Fig. S4 shows oxygen sites surrounding the Bi(2) cation, which lies at the surface of fluorite-like block. These oxygen sites are assumed to take part in ionic conductivity *via* an inter-planar pathway. As shown in Fig. S4a, Bi(2) at room temperature is surrounded by 6 mobile oxygen sites, 3 O(2) and 3 O(3). At 800 °C (Fig. S4b), 9 additional O(4) sites are present. In this case $g\alpha$ is equal to 1.5. However, these 9 sites can be separated into 3 groups of 3 sites, with sites in the same group too close to each other to be simultaneously occupied. This in itself would give $g_i = 3$. Even though technically it is possible for one site in all 3 of these groups to be occupied simultaneously, in practice it would mean that one Bi cation would be over-bonded to oxygen at the expense of other Bi cations. Such a case is highly unlikely and therefore the most likely scenario is that only 1 out of the 9 possible O(4) sites is occupied. Thus in effect, g_i is equal to 9 and because $g\alpha$ is equal to 1.5, α_i must be equal to 1/6. This value has significant consequences, because α_i denotes the maximum possible number of occupied interstitials (which, obviously, are never fully occupied). This would mean, that the interstitial concentration will be relatively low. This finds confirmation in experimental data. The maximum site occupancy fraction for O(4) at 800 °C was *ca.* 0.035. After recalculation as concentration per unit cell (fraction multiplied by site multiplicity, which is 18 and divided by total number of oxygen ions taking part in conduction processes per unit cell, namely O(2)+O(3), which is 7.5) the value is 0.084, which is well within the range of a "molten" state in this case.

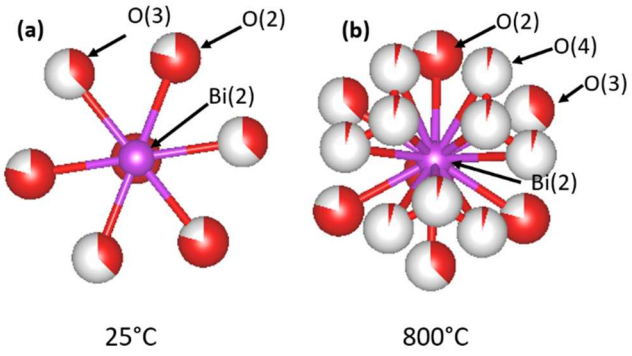

Fig. S4. Surroundings of Bi(2) atom presented along ab-plane in ordered (a) and disordered (b) state.

Table S2 summarizes the constant values used. The *z* value is a product of the number of oxygen ions taking part in conduction processes per unit cell and oxygen ion charge. *V* is the volume of the unit cell at room temperature and *e* and *k* denote electron charge and Boltzmann constant, respectively.

Table S2. Constants values used in cube-root model fitting.

z	V [cm^3]	e [C]	k [eV/K]	g_i	g_v	α_i	α_v
15	3.81×10^{-22}	1.602×10^{-19}	8.617×10^{-5}	9	1	1/6	1

Modification of conductivity formulae by volume expansion terms

Following Schmalzried approach, energy related parameters of the "cube-root" model in eq. (2)-(5), namely H_f, H_{m1}, H_{m2} and J parameters, were assumed to be linearly dependent on the thermal volume expansion $\varepsilon(T) = \frac{V(T)-V_0}{V_0}$:

$$H_{fv}(T) = H_{f0} - \Delta H_f \varepsilon(T) \quad \text{(S1)}$$

$$H_{m1v}(T) = H_{m10} - \Delta H_{m1} \varepsilon(T) \quad \text{(S2)}$$

$$H_{m2v}(T) = H_{m20} - \Delta H_{m2} \varepsilon(T) \quad \text{(S3)}$$

$$J_v(T) = J_0 - \Delta J \varepsilon(T) \quad \text{(S4)},$$

where H_{f0}, H_{m10}, H_{m20} and J_0 denote parameter values at a reference temperature (lowest temperature in the Arrhenius plot) and ΔH_f, ΔH_{m1}, ΔH_{m2}, ΔJ are related to the respective parameter changes with volume expansion. The temperature dependence of volume expansion coefficient ε(T) was calculated from extrapolated experimental data for $V(T)$ (Fig. 3) and shown in Fig. S5.

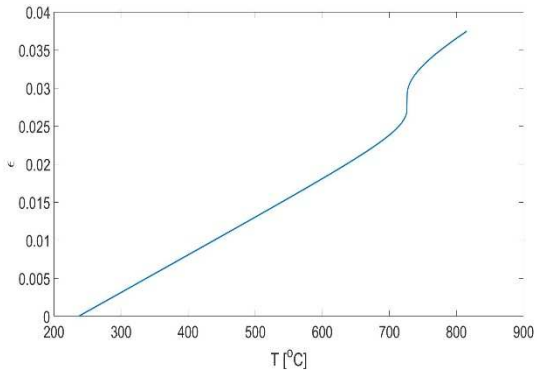

Fig. S5. Temperature dependence of thermal expansion coefficient $\boldsymbol{\varepsilon}$(T).

Conductivity data were modelled as a combination of inter-planar and intra-planar components, following the procedure described in the present paper, however H_f, H_{m1}, H_{m2} and J parameters in Eq. (2)-(5) were replaced with their volume-dependent equivalents H_{fv}, H_{m1v}, H_{m2v} and J_v as introduced in Eq. (S1)-(S4). Results of the fitting are presented in Fig. S6 and Table S3, showing that introduction of volume expansion correction terms ("modified"

fit) results in only a minimal difference compared to the “unmodified” fit (without volume change terms).

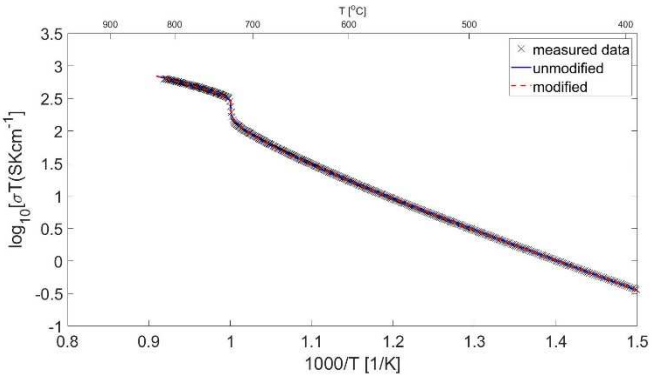

Fig. S6. Total conductivity data fitted with “modified” and “unmodified” “cube-root” models.

Table S3. Fitting parameters obtained for “modified” and “unmodified” models.

Parameter	Unmodified	Modified
H_{m1} [eV]	0.9043	0.9044
ΔH_{m1} [eV]	-	0.0116
σ_0 [S K cm^2 C^{-1}]	373.2	373.6
H_f [eV]	1.5055	1.5072
ΔH_f [eV]	-	0.0033
ΔS_{f0} /k	5.781	5.788
J [eV]	1.775	1.775
ΔJ [eV]	-	0.0026
H_{m2} [eV]	0.4807	0.4811
ΔH_{m2} [eV]	-	0.0042
μ_0 [S K cm^2 C^{-1}]	103.1	103.2
n	2.333	2.336
MSE	8.03×10^{-5}	8.14×10^{-5}